

Functional renormalization group treatment of the 0.7 analog in quantum point contacts

Lukas Weidinger, Christian Schmauder, Dennis H. Schimmel, and Jan von Delft
 Arnold Sommerfeld Center for Theoretical Physics and Center for NanoScience,
 Ludwig-Maximilians-Universität München, Theresienstrasse 37, D-80333 München, Germany



(Received 17 May 2018; published 7 September 2018)

We use a recently developed fRG method (extended Coupled-Ladder Approximation) to study the 0.7 analog in quantum point contacts, arising at the crossing of the first and second band at sufficiently high magnetic fields. We reproduce the main features of the experimentally observed magnetic field dependence of the conductance at the 0.7 analog, using a QPC model with two bands and short-range interactions. In particular, we reproduce the fact that this dependence is qualitatively different, depending on whether the analog is approached from higher or lower magnetic fields. We show that this effect can be explained qualitatively within a simple Hartree picture for the influence of the lowest electrons.

DOI: [10.1103/PhysRevB.98.115112](https://doi.org/10.1103/PhysRevB.98.115112)

I. INTRODUCTION

In quasi-one-dimensional structures, such as quantum wires or quantum point contacts (QPCs), an in-plane magnetic field induces a Zeeman splitting of different spin subbands. When this splitting equals the one-dimensional level spacing introduced by the lateral confinement of the structure, one finds crossing features similar to the 0.7 anomaly, as observed at zero magnetic field. Therefore, these features are called 0.7 analogs [1]. The most prominent of these 0.7 characteristics is the development of a shoulderlike structure in the conductance with increasing magnetic fields. In Fig. 1, one can see this shoulder in the original 0.7 regime (dashed ellipse) as well as the similar feature at the 0.7 analog (solid ellipse). The apparent similarities have intertwined the explanation attempts of 0.7 anomaly and 0.7 analogs, prominently featuring spontaneous spin-polarization [2], and quasilocalized states [3].

However, despite observed similarities, there are also features specific to the 0.7 analog that have no counterpart for the 0.7 anomaly. A striking example is the asymmetry in the magnetic field dependence of the conductance, depending on whether the analog is approached from higher or lower fields, see Fig. 1, which is an annotated version of Fig. 1 in Ref. [1]. While the 0.7 analog resembles the 0.7 anomaly at higher magnetic fields (green curve), the conductance curves at lower fields (red curve) are much more symmetric and show no sign of a 0.7 shoulder.

Some years ago, an interpretation of the 0.7 anomaly was introduced in Ref. [4] that traces its origins back to the structure of the noninteracting van Hove ridge in the local density of states. This interpretation has been supported by direct conductance calculations of the QPC via the functional renormalization group (fRG). Following this approach, we use here a recently developed extended coupled-ladder approximation (eCLA) fRG scheme [5] to study the features of the 0.7 analog at the crossing of the $1\uparrow$ and $2\downarrow$ spin subbands of a QPC, working out the similarities and differences between 0.7 analog and 0.7 anomaly.

We argue that the 0.7 analog physics can be explained in a similar manner as the 0.7 anomaly, evoking a smeared van Hove singularity in the local density of states. However, the effects of the electrons in the lowest spin subband are of critical importance. We demonstrate that these electrons cause the above-mentioned asymmetry in the magnetic field dependence of the conductance and study its dependence on the ratio of intra- to interband interaction strength.

II. THEORETICAL MODEL AND METHOD

A. Model

Since our goal is a qualitative understanding of the 0.7 analog physics, we use here the simplest model that should be able to give us the relevant features. We model the lowest two bands of the QPC via one-dimensional spinful tight-binding chains with an intra- and interband short-ranged interaction. The external magnetic field is modeled by a Zeeman term, splitting the energies of spin up and spin down electrons. We point out that, in experiments, one observes additionally to the Zeeman effect also a diamagnetic shift with increasing magnetic field. This shift is understood analytically [6], and is expected not to be relevant for the qualitative physics of interest here [1]. Therefore, we will omit this effect in the present qualitative study, and concentrate on the physics caused by the interactions. Our Hamiltonian will thus be of the form

$$\begin{aligned}
 H = & -\tau \sum_{i,s,\sigma} [c_{i,s\sigma}^\dagger c_{i+1,s\sigma} + \text{H.c.}] + \sum_{i,s,\sigma} V_{i,s\sigma} n_{i,s\sigma} \\
 & + \sum_{i,s} U_{i,s}^{\text{intra}} n_{i,s\uparrow} n_{i,s\downarrow} + \sum_{i,\sigma_1,\sigma_2} U_i^{\text{inter}} n_{i1\sigma_1} n_{i2\sigma_2}, \quad (1)
 \end{aligned}$$

where $c_{i,s\sigma}$ annihilates an electron at site i in band s with spin $\sigma \in \{+, -\} = \uparrow, \downarrow$, and $n_{i,s\sigma} = c_{i,s\sigma}^\dagger c_{i,s\sigma}$ is the corresponding number operator. In our calculations, we will use the hopping amplitude τ as unit of energy, i.e., we measure the on-site energy, $V_{i,s\sigma}$, as well as the intraband interaction, $U_{i,s}^{\text{intra}}$, and the interband interaction, U_i^{inter} , in units of τ . Within a

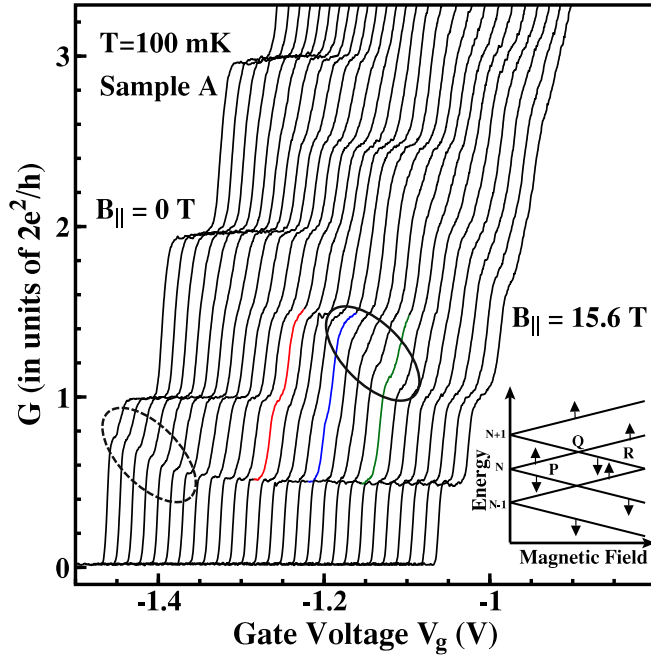


FIG. 1. Figure 1 of Ref. [1] with some additional annotations. As a guide for the eye, we colored three curves: The analog of the zero-field conductance step as well as two curves at magnetic fields $\Delta B = \pm 2.4 T$ above (green) and below (red) of the analog of the zero-field conductance step. The 0.7 anomaly is indicated by the dashed ellipse, that of its analog by the solid one. Clearly this 0.7-like behavior is only present if the analog is approached from above.

central region, $i \in [-N, N]$, we use the following form for the potential term:

$$V_{is\sigma} = V_g \exp\left[-\frac{(i/N)^2}{1 - (i/N)^2}\right] + V_s^{\text{off}} + \sigma \frac{B}{2}. \quad (2)$$

Here the first summand leads to a quadratic barrier top in the middle of the QPC with curvature $\Omega_x = 2\sqrt{V_g\tau}/N$ and corresponding characteristic length $l_x = a\sqrt{\tau/\Omega_x}$, with a being the lattice constant. The second term constitutes the band offset (we choose $V_1^{\text{off}} = 0$, and therefore use the abbreviation $V^{\text{off}} := V_2^{\text{off}}$) and the third term is the Zeeman splitting. To illustrate these settings, we have plotted the potential structure in Fig. 2.

Analogous to Ref. [4], we take both V_g as well as U_{is}^{intra} , and U_i^{inter} to be zero outside of the central region, where we thus have two noninteracting tight-binding leads with the site independent energy offset

$$V_{is\sigma} = V_s^{\text{off}} + \sigma \frac{B}{2}. \quad (3)$$

Those can be integrated analytically and their contribution absorbed in the self-energy Σ of the central region. Note that this contribution will, however, depend on V_s^{off} , as well as B . The short-ranged interactions U_{is}^{intra} and U_i^{inter} are treated as free parameters, chosen as site independent within the middle of the central region, and reduced smoothly to zero at its edges. All our calculations will be carried out in thermal equilibrium at zero temperature, implying that all states below the chemical potential μ are filled, all states above are empty.

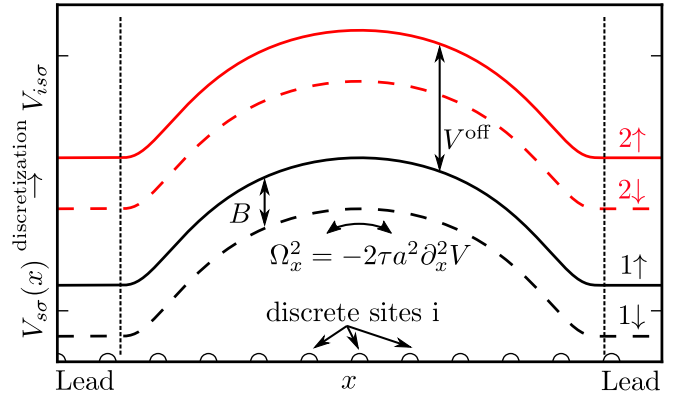


FIG. 2. Schematic illustration of the potential structure for the two spin-split bands, as given by Eq. (2). Note that the curvature of the barrier, Ω_x , is the same for all four subbands.

Our typical observable will be the linear response conductance through the system, and its dependence on the chemical potential μ , as well as on the magnetic field B .

Note that to keep things simple and clear, we have made here several simplifying assumptions. We omit any hopping terms between the two bands, keep the offset between the bands a site independent constant throughout the whole system (in particular the barrier curvature for both bands is the same) and omit any longer-ranged interactions. Furthermore, in all our calculations we will keep V_g constant and vary μ instead. In terms of the Fermi energy on the central site, $\epsilon_F = \mu - V_g$, this is the same as varying V_g with constant μ , but has the advantage that the bare curvature $\Omega_x(V_g)$ of the barrier does not change.

B. Method

To determine the interaction-induced self-energy, Σ , and two-particle vertex, γ , we use the recently introduced eCLA fRG scheme [5] within a static implementation. This scheme was originally designed to treat longer-ranged interactions. It enables the treatment of our two-band model, since it is possible to map the Hamiltonian Eq. (1) onto a one-dimensional chain model with longer-ranged interactions. For this, we simply interleave the different bands, as sketched in Fig. 3, leading to a new effective one-dimensional Hamiltonian, containing interactions between neighboring sites:

$$H_{\text{eff}} = -\tau \sum_{j,\sigma} [c_{j\sigma}^\dagger c_{j+2\sigma} + \text{H.c.}] + \sum_{j,\sigma} \tilde{V}_{j\sigma} n_{j\sigma} + \sum_j \tilde{U}_j^{\text{intra}} n_{j\uparrow} n_{j\downarrow} + \sum_{j,\sigma_1,\sigma_2} \tilde{U}_{2j}^{\text{inter}} n_{2j\sigma_1} n_{2j+1\sigma_2}. \quad (4)$$

Here the new index is given by $j = 2i + s - 1$ ($s = 1$ is band 1, $s = 2$ is band 2), and the coefficients are $\tilde{V}_{j\sigma} = V_{is\sigma}$, $\tilde{U}_j^{\text{intra}} = U_{is}^{\text{intra}}$, and $\tilde{U}_j^{\text{inter}} = U_i^{\text{inter}}$. We will sometimes use $\alpha = (s, \sigma)$ as composite species index.

This Hamiltonian is now in a form suitable for the eCLA approach. Without going into detail, we just point out that this method depends crucially on a dimensionless parameter, L , called the feedback length in Ref. [5], which determines the spatial extent of the renormalized vertex, γ . This L has to

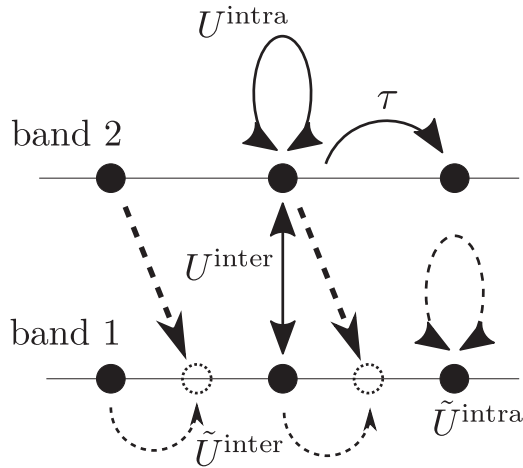


FIG. 3. Schematic procedure of interleaving the two bands. Note that in the effective chain, we get again on-site, as well as anisotropic nearest neighbor interactions.

be chosen large enough to reach convergence, and we will comment on the convergence properties in the beginning of the next section.

Finally, the calculation of the zero-temperature linear response conductance, $g = \frac{h}{2e^2} \frac{\partial I}{\partial V}$, from the self-energy obtained with our fRG method, is carried out via the formula [7–9]

$$g = \frac{1}{2} \sum_{\sigma,s} |2\pi\rho^{\sigma s}(\mu + i0^+)\mathcal{G}_{-NN}^{\sigma s}(\mu + i0^+)|^2, \quad (5)$$

where $\rho^{\sigma s}$ is the density of states on the first lead site for spin σ and band s , and $\mathcal{G}_{-NN}^{\sigma s}$ is the propagator for an electron in band s with spin σ from the leftmost to the rightmost site of the central region.

III. RESULTS

We use the following general settings in this section: The band offset is chosen as $V^{\text{off}} = 0.1\tau$ and $N = 30$, therefore the total number of spatial sites in the central region is $N_{\text{tot}} = 61$ and correspondingly the total number of effective sites in Eq. (4) is $N_{\text{eff-tot}} = 122$. Furthermore, except for Fig. 6, we set $V_g = 0.5\tau$, implying a curvature $\Omega_x \approx 0.05\tau$.

In Fig. 4(a), we show the noninteracting, as well as the fully L -converged conductance for our two-band model, with the simplest nontrivial interaction configuration, $U_{is}^{\text{intra}} = U_i^{\text{inter}} = 0.7\tau$. These values correspond to a typical value for the onsite interactions in a one-band QPC used in Ref. [4]. The main changes caused by the interaction are the slightly more asymmetric shape of the conductance steps, and the shift to larger chemical potentials observed for the second step. Qualitatively, this shift is caused by the additional interaction energy between the electrons of the two bands (Hartree shift).

A. Convergence in L

Before we proceed, let us first discuss the convergence of our method with respect to the feedback length L . For a one-band QPC with onsite interactions, L has to be of the

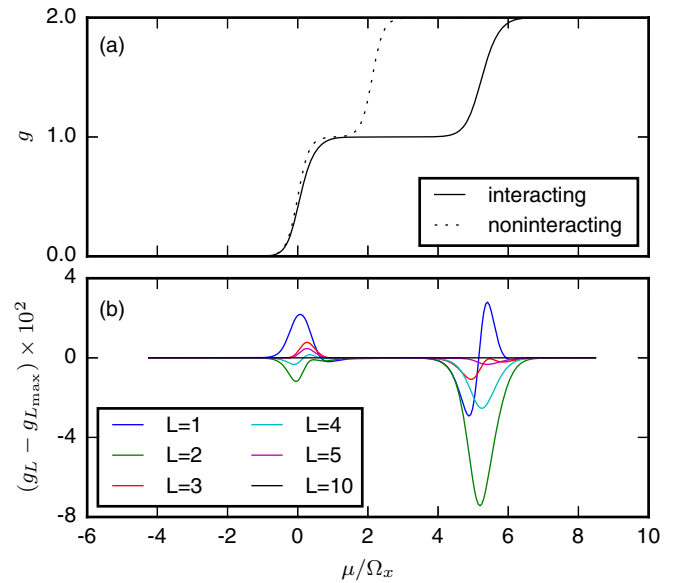


FIG. 4. (a) Conductance g for the non- as well as the interacting system for $L = 10$ as function of μ . (b) Difference between the conductance for several L values to the converged result (at $L = L_{\text{max}} = 10$). We see that convergence is achieved around $L = 5$.

order of the characteristic length of the harmonic barrier top to achieve convergence: $L \approx l_x/a$, with the lattice spacing a . For our interleaved two-band system, we would thus simply expect $L \approx 2l_x/a$, since the effective distance between two points of the same band is doubled and the effect of the now-finite interaction range on the convergence should be negligible, since the introduced nearest-neighbor interaction is still much shorter than l_x . In Fig. 4(b), the convergence behavior in L is shown. We see that the convergence for the two-band model is achieved around $L \approx 5$. Since in our system $l_x \approx 4.6a$, this shows that L can in fact be chosen smaller than the naive guess, $L \approx 2l_x/a$, indicating stabilizing feedback effects between the two bands.

As a side remark, we point out that the finite extent of the renormalized vertex beyond the lowest value (i.e., $L > 1$) is actually important to treat the screening properties between the two bands. This will be seen in the next section when we study the magnetic-field dependence of the conductance.

B. Small magnetic field

Before we look at the 0.7 analog, we want to take a brief look at the properties of the conductance at magnetic fields much smaller than the band spacing, $B \ll V^{\text{off}}$, see Fig. 5, solid curves.

There are two main observations we make here: First, we see that the magnetic-field dependence of the second step is more symmetric, indicating that the interaction of the electrons in the second band is screened by electrons in the first band. Second, we see that the second conductance step is broader than the first one. This feature can be qualitatively understood in a simple Hartree picture: While increasing μ during the second step, electrons are still filling up the lowest band, leading to an increasing Hartree shift for the

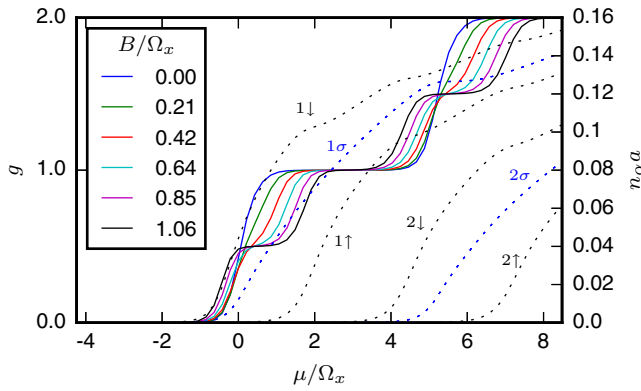


FIG. 5. Solid curves: Conductance at low magnetic fields, i.e., with $B \ll V^{\text{off}} = 0.1\tau \approx 2.12\Omega_x$ and $U^{\text{intra}} = U^{\text{inter}} = 0.7\tau$. The second spin-split double step is more symmetric and broader than the first. Dotted curves: Spin resolved electron densities n_α on the central QPC site for $B/\Omega_x = 0$ (blue) and $B/\Omega_x = 1.06$ (black). Note the damping that appears in n_α whenever a different particle species enters the QPC.

electrons in the higher band. As a result, the second step gets broadened.

To further validate this explanation, we can compute an estimate for the observed broadening via

$$\Delta E = U^{\text{inter}}(\Delta n_{1\downarrow} + \Delta n_{1\uparrow})a, \quad (6)$$

where $\Delta n_{1\sigma}$ is the total change of the first-band spin- σ density at the center of the QPC during the second conductance step. Instead of considering a “pure” Hartree effect where one would use for $n_{1\sigma}$ only the density of a system without interband interaction, we can improve on that by using the actual fully interacting densities that we obtained from our fRG calculation. These densities are given by

$$n_i^\alpha = \int_{-\infty}^{\mu} d\omega A_i^\alpha(\omega), \quad (7)$$

where the local density of states at site i for particle species α , $A_i^\alpha(\omega) = -\text{Im} G_{ii}^\alpha(\omega)/\pi$ is given by the imaginary part of the fully interacting retarded electron propagator $G_{ii}^\alpha(\omega)$. It is instructive to take a quick look at these densities themselves: In Fig. 5, we have plotted the density for the different particle species in the center of the QPC, $n_\alpha \equiv n_0^\alpha$ (dotted curves). Each time a new particle species enters the QPC, the increase of any other species n_α is slowed down, or “damped,” due to the corresponding interaction. The damping of $n_{1\sigma}$ during the second conductance step will lead (starting in second order in U^{inter}) to a reduction of the pure Hartree broadening of that step. We see that the damping in $n_{1\sigma}$ is most pronounced at $B = 0$, when both $n_{2\uparrow}$ and $n_{2\downarrow}$ particles enter the QPC at the same time. Correspondingly, the width of the second conductance step is only slightly larger than that of the first. On the other hand, for $B/\Omega_x = 1.06$, the damping in $n_{1\sigma}$ is relatively small, leading to a pronounced broadening of the second conductance step. Using Eq. (6), the effective Hartree broadening can be obtained from the change of the densities $n_{1\sigma}$ during the second conductance step. For example, in the $B/\Omega_x = 1.06$ case, the second conductance step occurs between $\mu/\Omega_x \approx 3.3$, with densities $n_{1\downarrow} \approx 0.12/a$, $n_{1\uparrow} \approx$

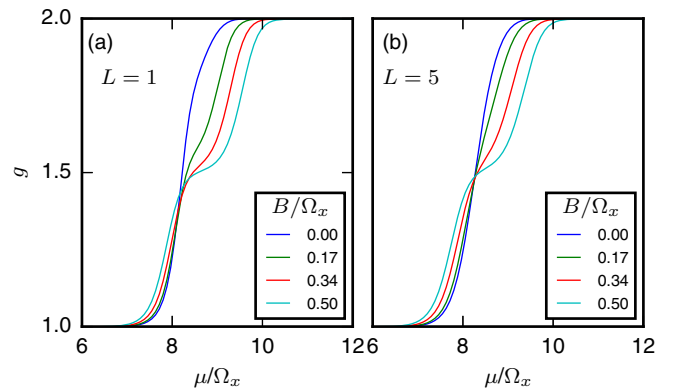


FIG. 6. Magnetic field dependence of the second conductance step. (a) $L = 1$, (b) $L = 5$. We see that the second conductance step is more symmetric in the $L = 5$ case, indicating a better screening of interactions in the second band.

$0.08/a$, and $\mu/\Omega_x \approx 7.8$, with densities $n_{1\downarrow} \approx 0.15/a$, $n_{1\uparrow} \approx 0.13/a$. Therefore, the effective Hartree broadening given by Eq. (6) is

$$\begin{aligned} \Delta E &\approx 0.7\tau \cdot [(0.15 - 0.12) + (0.13 - 0.08)] \\ &= 0.056\tau \approx 1.1\Omega_x. \end{aligned} \quad (8)$$

This result can be compared with the observed broadening of the second conductance step: The widths of the steps are $\Delta\mu_{\text{step 1}} \approx (2.4 - (-1.2))\Omega_x = 3.6\Omega_x$ and $\Delta\mu_{\text{step 2}} \approx (7.8 - 3.3)\Omega_x = 4.5\Omega_x$, leading to a relative broadening of $\Delta\mu_{\text{step 2}} - \Delta\mu_{\text{step 1}} \approx 0.9\Omega_x$, which is in qualitative agreement with Eq. (8). The effect that the electrons in the first band change the form of the second conductance step is quite generic and will be also encountered in the 0.7 analog case.

Here it is also interesting to look at the L -dependence of the conductance with various magnetic fields. Particularly for longer QPCs, where $l_x \gtrsim 5a$, the increase in L has a visible impact, see Fig. 6.

For $L = 1$, the second conductance step is very asymmetric, but becomes more symmetric with increasing L , due to the screening of the interaction in the second band instigated by electrons in the first band. The curvature, $\Omega_x \approx 0.03\tau$ ($V_g = 0.2\tau$), which we used here, is comparable to the one in a previous fRG study [10] of the two-band model. However, in that work, the results were not converged in L , therefore underestimating screening effects.

C. 0.7 analog at large magnetic field

Having studied the properties of the two-band model at low magnetic fields, we are now prepared to tackle the 0.7 analog. This analog appears at the crossing of the $1\uparrow$ and the $2\downarrow$ spin subbands at a magnetic field, $B = B_c$, which is of the order of the energy separation of the two bands V^{off} (determined by the confinement in the lateral direction). This situation resembles the situation given in the 0.7 anomaly, in the sense that two particle species are competing while trying to get through the QPC. Therefore, one might naively expect that the 0.7 analog shows the same features as the 0.7 anomaly. However, this is only partially true. While for

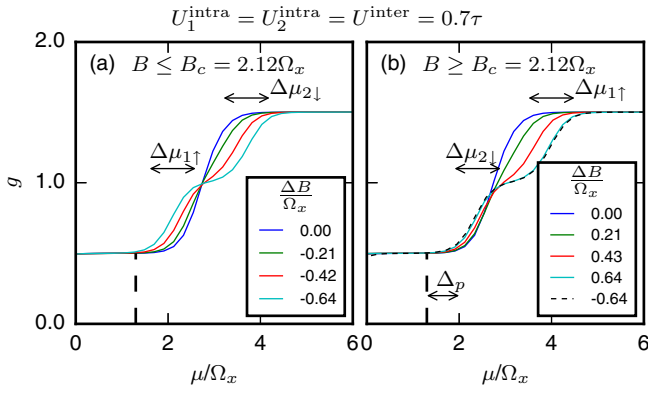


FIG. 7. (a) Conductance curves for $B \leq B_c = 0.1\tau \approx 2.12\Omega_x$ and (b) for $B \geq B_c$ at equal intra- and interband interaction strengths. In (b), the dotted curve is the manually shifted curve, $\Delta B/\Omega_x = -0.64$, from (a). We see that it has exactly the same form as the corresponding curve for $\Delta B/\Omega_x = 0.64$. The quantities $\Delta\mu_{1\uparrow}$, $\Delta\mu_{2\downarrow}$ measure the width of the corresponding half-steps and Δ_p indicates the pinch-off shift between $\Delta B < 0$ and $\Delta B > 0$, see also Fig. 8.

$\Delta B = B - B_c > 0$ the experimentally measured conductance shows the typical feature of 0.7 physics, namely the development of a shoulder with increasing magnetic field, this feature is missing for $\Delta B < 0$.

In trying to understand the underlying physics, we first start with the simplest interaction model, $U_{is}^{\text{intra}} = U_i^{\text{inter}} \equiv U = 0.7\tau$, which we already used in the last sections. Figure 7 shows the resulting conductance.

We make two main observations: First, the curves for $\Delta B < 0$ lie approximately symmetrically around the B_c curve, while the $\Delta B > 0$ curves do not. However, second, the actual shapes of corresponding curves, i.e., for $B = B_c - \Delta B$ and $B = B_c + \Delta B$, are very similar, they are just offset by different amounts.

This behavior can be understood by a similar argument as used for the broadening of the conductance step in the low magnetic field case above. As already mentioned, in a case with only $1\uparrow$ and $2\downarrow$ particles, the situation would be completely symmetric. Therefore the different behavior must stem from the other particles in the system. Since, in the analog case, the $2\uparrow$ spin subband lies much higher than the chemical potential and is therefore empty, the $1\downarrow$ particles must be responsible for the change of situation.

Both of our observations can be explained by taking the effect of the $1\downarrow$ electrons in a simple Hartree argument into account: The Hartree shift on particle species α induced by the $1\downarrow$ particles in the center of the QPC is given by $E_H^\alpha = U_\alpha n_{1\downarrow} a$, where U_α denotes the appropriate interaction (U^{intra} for $\alpha = 1\uparrow$, U^{inter} for $\alpha = 2\downarrow$). Assuming that the chemical potential μ is already far above the $1\downarrow$ van Hove ridge, $\mathcal{A}_{1\downarrow}(\omega) \approx \mathcal{A}_{1\downarrow}$ will be approximately constant, and the Hartree shift will be approximately of the form $E_H^\alpha \approx U_\alpha (n_{1\downarrow}^c + (\mu - b_{1\downarrow}) \mathcal{A}_{1\downarrow}) a$, with a constant $n_{1\downarrow}^c$ and the barrier top of the $1\downarrow$ particles given by $b_{1\downarrow} = V_g - \frac{B}{2}$. Leaving the other interactions aside for a moment, we can readily write down the μ - and B -dependence of the renormalized barrier

tops of the $1\uparrow$ and $2\downarrow$ particles:

$$\begin{aligned} b_{1\uparrow} &= V_g + \frac{B}{2} + E^{1\uparrow H}(B, \mu), \\ b_{2\downarrow} &= V_g + V^{\text{off}} - \frac{B}{2} + E^{2\downarrow H}(B, \mu). \end{aligned} \quad (9)$$

The qualitative behavior of this equations is shown in Fig. 8, and provides a good explanation for the observed phenomena: In contrast to the noninteracting case [Fig. 8(a)], we obtain for $U^{\text{intra}} = U^{\text{inter}}$ a pinch-off asymmetry, Δ_p , between the pinch-offs at magnetic fields above and below the analog, see Fig. 8(b). Taking into account the interaction between $1\uparrow$ and $2\downarrow$ (whose main effect is a broadening of the second half-step), this results in the more symmetric arrangement of the two half-steps around the crossing curve for $\Delta B < 0$, and to a more asymmetric situation in the $\Delta B > 0$ case. However, we see that the shape of corresponding curves is the same since the μ -width of the half-steps, $\Delta\mu_{1\uparrow}$ and $\Delta\mu_{2\downarrow}$, is equal.

If we compare this to experiment [1], we see that this setting reflects only partially the experimental situation: While the half-steps are indeed arranged more symmetrically for $\Delta B < 0$ than for the $\Delta B > 0$ case, also the form of the corresponding curves themselves differs substantially in experiment. For $\Delta B > 0$, the conductance curves are much more asymmetric in the μ behavior, developing a 0.7 analog plateau, while for $\Delta B < 0$ they are not. To analyze this quantitatively in our calculation, we introduce the ‘‘conductance asymmetry’’ $\Delta g(\mu) = g_m(\mu) - g(\mu)$, where $g_m(\mu)$ is the mirror image of $g(\mu)$ around the point $g(\mu)/g_0 = 1.0$ under reflection in both the horizontal and vertical direction. The more asymmetric the conductance curve is in μ , the larger gets the modulus of Δg . This is illustrated in Fig. 9(a). Figure 9(b) shows the dependence of this asymmetry Δg on the magnetic field. We see that contrary to the experiment the asymmetry is equally strong above and below the crossing value B_c .

This indicates that our description up to now lacks an important ingredient. We will argue in the following that this is due to the unphysical choice $U^{\text{intra}} = U^{\text{inter}}$. Generically, one would expect $U^{\text{inter}} < U_2^{\text{intra}} < U_1^{\text{intra}}$. The first statement is due to the smaller overlap of the transversal wave functions between different bands, the second because the transversal wave function in the second band is spread out wider than in the first band. Both effects lead to a weakening of the effective one-dimensional interaction strength. Estimates for the ratios of this different interaction strengths can be obtained in a similar manner as in Ref. [5], see Appendix, and yield $U_2^{\text{intra}}/U_1^{\text{intra}} \approx 0.77$ and $U^{\text{inter}}/U_1^{\text{intra}} \approx 0.36$. Keeping our previous U_1^{intra} fixed, this leads approximately to $U_2^{\text{intra}} = 0.5\tau$ and $U^{\text{inter}} = 0.3\tau$.

To investigate the influence of these differences in interaction strength, we proceed in two steps. In the ideal case where the analog region is well separated from the $2\uparrow$ conductance step, we expect that the influence of U_2^{intra} at the analog is not important, since the barrier for the $2\uparrow$ electrons is way above the chemical potential. Therefore, we will first keep U_2^{intra} equal to $U_1^{\text{intra}} = 0.7\tau$ and investigate the influence of a reduction of $U^{\text{inter}} = 0.3\tau$ alone. In Fig. 10, we show the resulting conductance curves. Again, we encounter a pinch-off shift of the higher spin subband steps; however, due to

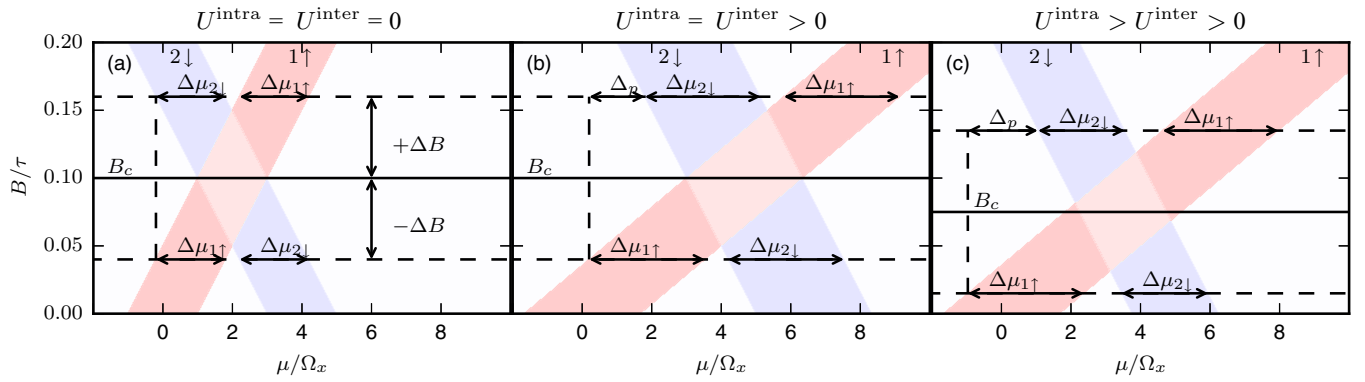


FIG. 8. Schematic behavior of the Hartree renormalized barriers of the $1\uparrow$ (red) and $2\downarrow$ (blue) particles as function of μ and B . The colored regions indicate where $|b_\alpha - \mu| < \Omega_x/2$, i.e., the regions within which the conductance steps occur. (a) Noninteracting case: $B_c = V^{\text{off}}$, no pinch-off asymmetry, no shape asymmetry. (b) $U^{\text{intra}} = U^{\text{inter}}$: $B_c = V^{\text{off}}$, pinch-off asymmetry ($\Delta_p > 0$), no shape asymmetry. (c) $U^{\text{intra}} > U^{\text{inter}}$: $B_c < V^{\text{off}}$, pinch-off asymmetry ($\Delta_p > 0$) and shape asymmetry ($\Delta\mu_{1\uparrow} > \Delta\mu_{2\downarrow}$).

the different interaction strengths, the crossing point B_c is now shifted, too. More importantly, we see that in addition to the pinch-off asymmetry, also the shape of corresponding curves for $\Delta B < 0$ and $\Delta B > 0$ differ, the curves for $\Delta B < 0$ being much more symmetric than the $\Delta B > 0$ curves. This is the behavior also observed in experiment and for further reference, we will call it the “shape asymmetry.”

These features can be readily explained with our Hartree picture for the renormalized barrier positions Eq. (9). Their behavior for $U^{\text{intra}} > U^{\text{inter}}$ (i.e., the Hartree shift for the $2\downarrow$ subband is smaller than for the $1\uparrow$ subband) is shown in Fig. 8(c). We see two immediate effects: (i) The $2\downarrow$ subband is shifted to lower values of μ and therefore the value of the magnetic field B_c , where the two subbands cross is shifted to lower magnetic fields, as encountered in the Fig. 10, and (ii) the width $\Delta\mu_{2\downarrow}$ of the $2\downarrow$ half-step is decreased, therefore yielding the shape asymmetry: For $\Delta B < 0$, the first half-step ($1\uparrow$) is broader than the second half-step ($2\downarrow$), thus counteracting the asymmetry introduced by the interband interaction between the competing particles themselves and leading in

total to a more symmetric curve. For $\Delta B > 0$, the effect is reversed, leading to a more asymmetric curve.

Furthermore, Fig. 8(c) exhibits a third interesting, albeit less pronounced feature: Due to the smaller interaction with the lowest electrons, the μ -width of the $2\downarrow$ -strip is smaller than the width of the $1\uparrow$ -strip and therefore the two middle corners of the intersecting diamond [light pink region in

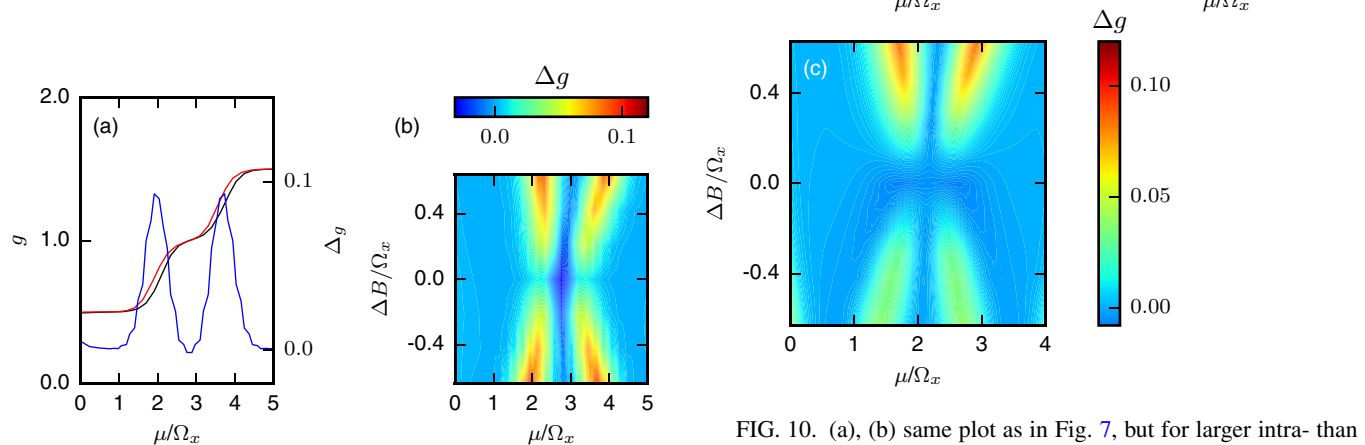


FIG. 9. Illustration of the asymmetry in μ . (a) Conductance curve $\Delta B/\Omega_x = -0.64$ from Fig. 7 (black), together with its mirror image (red) under inversion around the $g = 1.0$ point, and the difference Δg between the two curves (blue). (b) Colorplot of Δg as a function of magnetic field and chemical potential. We see that the strength of the curve asymmetry is symmetric around B_c .

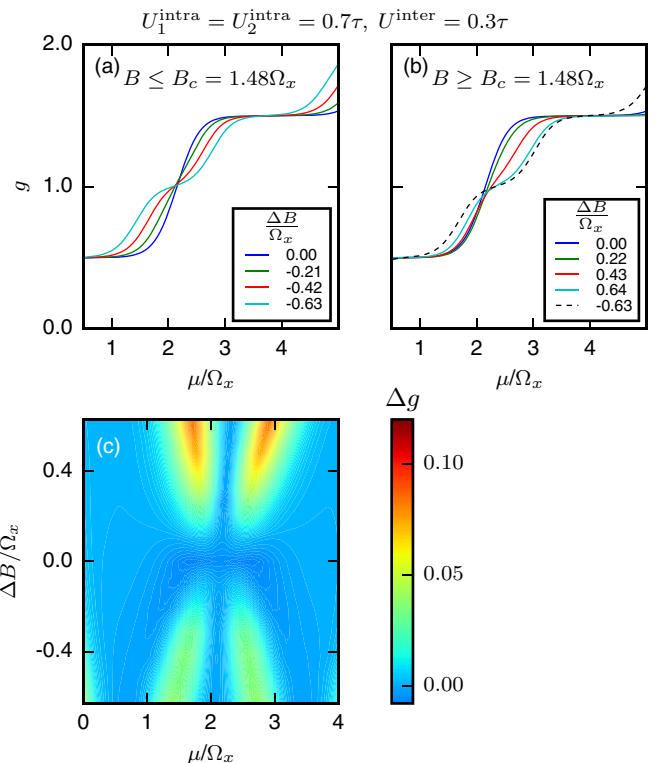


FIG. 10. (a), (b) same plot as in Fig. 7, but for larger intra- than interband interaction ($U_{1,2}^{\text{intra}} = 0.7\tau$, $U^{\text{inter}} = 0.3\tau$), resulting in $B_c \approx 1.48\Omega_x$. In (b), the dashed curve is again the $\Delta B/\Omega_x = -0.63$ curve from (a), manually shifted such that it intersects the corresponding $\Delta B/\Omega_x = 0.64$ curve at the $g/g_0 = 1$ point. However, contrary to Fig. 7(b), the shape of the two curves does not coincide. (c) Colorplot of the shape asymmetry. In contrast to Fig. 9(b), we see that the asymmetry is clearly stronger for $\Delta B > 0$ than for $\Delta B < 0$.

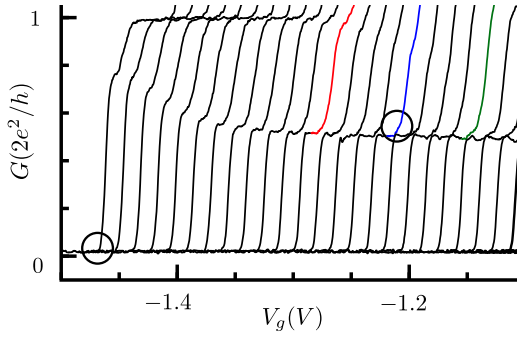


FIG. 11. Zoom of Fig. 1. Note the slight kink that occurs at the onset of the blue 0.7 analog curve compared to the steep onset of the $B = 0$ curve (circled areas).

Fig. 8(c)] do not lie on the B_c line, but are shifted slightly upward or downward from it. Directly at the B_c line, i.e., at the 0.7 analog, the broader $1\uparrow$ and the thinner $2\downarrow$ steps superimpose symmetrically, which leads to a conductance curve with slightly less steep parts at the onset and at the end in μ direction. Since the Hartree picture we use in Fig. 8 takes only the interaction with the $1\downarrow$ electrons and not the interaction between the $1\uparrow$ and $2\downarrow$ electrons themselves into account, we expect this small effect to be most prominent at the onset of the second conductance step. In the experimental data, one might interpret the slight kink that occurs at the onset of the blue 0.7 analog step, compared to the smooth $B = 0$

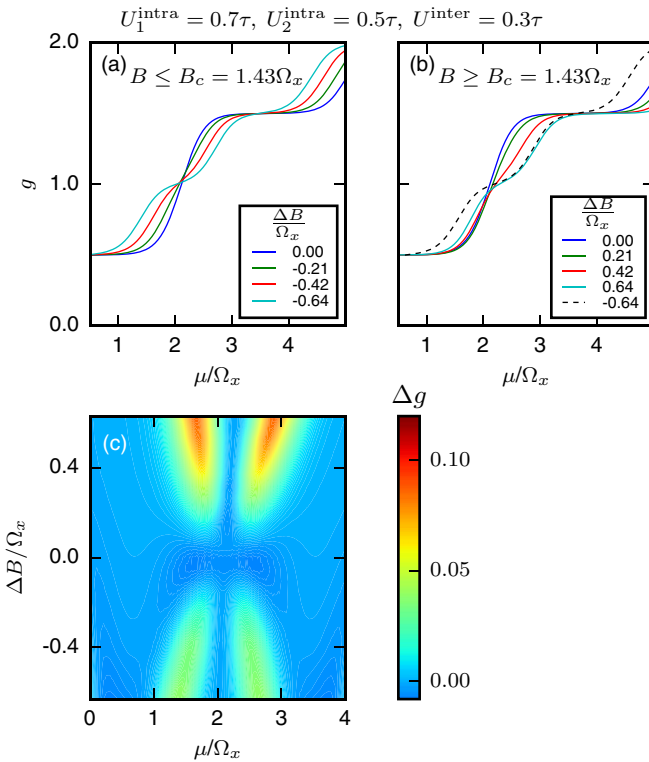


FIG. 12. (a), (b) same plot as in Figs. 7(a) and 7(b) and Figs. 10(a) and 10(b), but for three different interactions: $U_1^{\text{intra}} = 0.7\tau$, $U_2^{\text{intra}} = 0.5\tau$, and $U^{\text{inter}} = 0.3\tau$. In comparison to Fig. 10, the crossing point is slightly reduced to $B_c = 1.43\Omega_x$; however, the asymmetry persists. (c) Colorplot of the shape asymmetry, which stays very similar to Fig. 10(c).

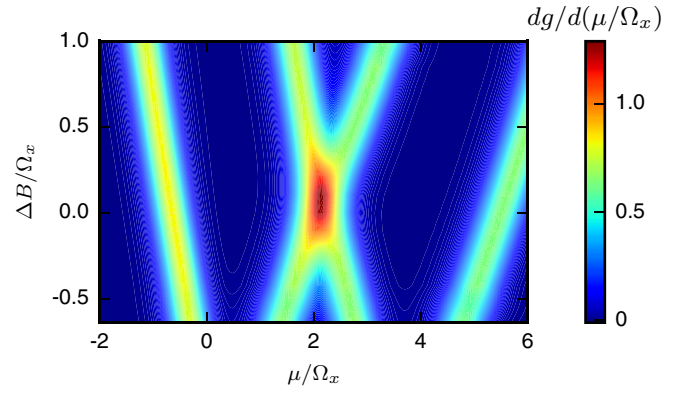


FIG. 13. Colorplot of the transconductance as function of B and μ . Note the more pronounced asymmetry at the $\Delta B > 0$ than the $\Delta B < 0$ part of the crossing region.

curve, as a result of the described effect, compare circled onsets in Fig. 11. However, this feature is quite weak and could also be caused by other causes, e.g., a gate-dependent deformation of the QPC potential. Furthermore, we do not observe any visible effect of this kind in our fRG calculations, see Fig. 10.

As a last step, we finally also reduce $U_2^{\text{intra}} = 0.5\tau < U_1^{\text{intra}}$. The results are shown in Fig. 12. We see that the reduction of U_2^{intra} slightly shifts the crossing point B_c to lower values of the magnetic field; however, the shape asymmetry introduced by the lowering of U^{inter} stays intact. Thus, in terms of Fig. 8, the net effect of the reduction of U_2^{intra} is simply a slight shift of the blue $2\downarrow$ barrier top position stripe to the left, i.e., to lower values of μ , without changing its slope.

D. Limitations

A limitation of our static zero temperature calculation is that we have no access to inelastic processes. We suspect that this leads to a main difference between our results and experimental observations, namely that we do not see a pronounced finite temperature plateau in the conductance. This can be clearly seen by comparing the transconductances $dg/d\mu$, see Fig. 13, where we do not observe the “gap” at $\Delta B > 0$ as in the experimental data, cf. Fig. 2(a) in Ref. [1] or Fig. 1(b) in Ref. [11]. However, we also see in the transconductance, that for $\Delta B > 0$ the broadening of the conductance curve in the second half-step is more pronounced than for $\Delta B < 0$, where the half-steps are more symmetric in position as well as slope.

IV. CONCLUSION

We have studied the 0.7 analog in QPCs using a two-band model with intra- and interband onsite interactions and found that we could qualitatively reproduce the magnetic field dependence of the conductance around the analog. In particular, we could reproduce the asymmetry in the conductance, depending on whether the analog is approached from higher or lower magnetic fields.

Due to our use of a static fRG scheme, we were not able to investigate finite temperature properties of the analog, which is an interesting direction for further research.

ACKNOWLEDGMENTS

We thank Prof. Dr. D. A. Ritchie for letting us use Fig. 1 from their publication [1]. Furthermore, we gratefully acknowledge support from the Cluster of Excellence Nanosystems Initiative Munich.

APPENDIX: ESTIMATE OF THE QPC INTERACTION STRENGTHS

Following the approach of Ref. [12], we calculated in Ref. [5] the intraband interaction for a QPC with a single band

that resulted from a screened Coulomb interaction. This was done by taking only the ground state ϕ_1 of the transversal y direction (in the two-dimensional electron gas plane) into account. Since the confinement in y direction can be approximated by a harmonic potential, ϕ_1 is simply the ground state of a harmonic oscillator. In a QPC with two bands, we additionally also take the first excited state of the harmonic y confinement into account. The computation of the resulting matrix elements for the interaction between two effective one-dimensional states at x_0 and x_1 can be done analogously to the one-dimensional case and yields in terms of integrals over the relative coordinate r in the transversal direction:

$$U_1^{\text{intra}}(x_0, x_1) = (l_y^2(x_0) + l_y^2(x_1))^{-\frac{1}{2}} \int dr g(r), \quad (\text{A1})$$

$$U_2^{\text{intra}}(x_0, x_1) = (l_y^2(x_0) + l_y^2(x_1))^{-\frac{9}{2}} \int dr g(r) [3l_y^2(x_0)l_y^2(x_1)(l_y^2(x_0) + l_y^2(x_1))^2 + (l_y^2(x_0) + l_y^2(x_1)) \times (l_y^4(x_0) - 4l_y^2(x_0)l_y^2(x_1) + l_y^4(x_1))r^2 + l_y^2(x_0)l_y^2(x_1)r^4)], \quad (\text{A2})$$

$$U^{\text{inter}}(x_0, x_1) = (l_y^2(x_0) + l_y^2(x_1))^{-\frac{5}{2}} \int dr g(r) [l_y^4(x_1) + l_y^2(x_0)(l_y^2(x_1) + r^2)], \quad (\text{A3})$$

where $l_y(x)$ is the (x dependent) characteristic length in y direction, e the electron charge, κ the dielectric constant, and $g(r)$ (which consists of the screened Coulomb interaction, as well as the lateral confinement) is given by

$$g(r) = \frac{e^2}{\kappa} \left[\frac{1}{\sqrt{(x_0 - x_1)^2 + r^2}} - \frac{1}{\sqrt{(x_0 - x_1)^2 + r^2 + l_s^2}} \right] e^{-r^2/(2(l_y^2(x_0) + l_y^2(x_1)))}, \quad (\text{A4})$$

where l_s is the screening length. All these contributions are logarithmically divergent for $x_0 \rightarrow x_1$. In this work, we make the simplest approximation and ignore the position dependence of the U 's, by setting them to their value in the QPC center. Then we obtain for the ratios of the different effective interaction strengths used in Sec. III C:

$$\frac{U_2^{\text{intra}}}{U_1^{\text{intra}}} = \lim_{x_1 \rightarrow 0} \frac{U_2^{\text{intra}}(0, x_1)}{U_1^{\text{intra}}(0, x_1)} \approx 0.77, \quad (\text{A5})$$

$$\frac{U^{\text{inter}}}{U_1^{\text{intra}}} = \lim_{x_1 \rightarrow 0} \frac{U^{\text{inter}}(0, x_1)}{U_1^{\text{intra}}(0, x_1)} \approx 0.36, \quad (\text{A6})$$

where in the last step we used a ratio $l_s/l_y(0) = 3$, which could, for example, be realized in a QPC with $l_s = 50$ nm and $l_y = 17$ nm, which corresponds in a GaAs 2DEG to a curvature $\Omega_y = 2$ meV.

-
- [1] A. C. Graham, K. J. Thomas, M. Pepper, N. R. Cooper, M. Y. Simmons, and D. A. Ritchie, *Phys. Rev. Lett.* **91**, 136404 (2003).
- [2] K.-F. Berggren, P. Jaksch, and I. Yakimenko, *Phys. Rev. B* **71**, 115303 (2005).
- [3] Y. Meir, *J. Phys.: Condens. Matter* **20**, 164208 (2008).
- [4] F. Bauer, J. Heyder, E. Schubert, D. Borowsky, D. Taubert, B. Bruognolo, D. Schuh, W. Wegscheider, J. von Delft, and S. Ludwig, *Nature* **501**, 73 (2013).
- [5] L. Weidinger, F. Bauer, and J. von Delft, *Phys. Rev. B* **95**, 035122 (2017).
- [6] F. Stern, *Phys. Rev. Lett.* **21**, 1687 (1968).
- [7] S. Datta, *Electronic Transport in Mesoscopic Systems*, Cambridge Studies in Semiconductor Physics (Cambridge University Press, Cambridge, 1997).
- [8] A. Oguri, *J. Phys. Soc. Jpn.* **70**, 2666 (2001).
- [9] D. Schimmel, Transport through Inhomogeneous Interacting Low-Dimensional Systems, Ph.D. thesis, Ludwig-Maximilians-Universität, München, 2017.
- [10] K. Eissing, Functional Renormalization Group Applied to a Multimode Quantum Point Contact, Master's thesis, LMU München, 2013.
- [11] A. C. Graham, D. L. Sawkey, M. Pepper, M. Y. Simmons, and D. A. Ritchie, *Phys. Rev. B* **75**, 035331 (2007).
- [12] A. M. Lunde, A. D. Martino, A. Schulz, R. Egger, and K. Flensberg, *New J. Phys.* **11**, 023031 (2009).